Title

Quantum Entanglement Filtering: A PET feasibility study in imaging dual-positron and prompt gamma emission via Monte Carlo simulation.

Journal

IEEE Transactions on Radiation and Plasma Medical Sciences, 8(8)

ISSN

2469-7311

Authors

Romanchek, Gregory

Shoop, Greyson

Gholami, Kimia

et al.

Publication Date

2024-11-01

DOI

10.1109/trpms.2024.3388872

Peer reviewed

HHS Public Access

Author manuscript

IEEE Trans Radiat Plasma Med Sci. Author manuscript; available in PMC 2024 November 06.

Published in final edited form as:

IEEE Trans Radiat Plasma Med Sci. 2024 November ; 8(8): 916–925. doi:10.1109/trpms.2024.3388872.

Quantum Entanglement Filtering: A PET feasibility study in imaging dual-positron and prompt gamma emission via Monte Carlo simulation

Gregory Romanchek[1], **Greyson Shoop**[2], **Kimia Gholami**[2], **Emily Enlow**[2], **Shiva Abbaszadeh**[2,*]

[1]University of Illinois at Urbana-Champaign, Nuclear, Plasma, and Radiological Engineering, Champaign, 61820, USA

[2]University of California, Santa Cruz, Electrical and Computer Engineering, Santa Cruz, 95064, USA

Abstract

In this article, we investigate quantum entanglement (QE) filtering to address the challenges in multi-isotope positron emission tomography (PET) or in PET studies utilizing radiotracers with dual- positron and prompt gamma emissions. Via GATE simulation, we demonstrate the efficacy of QE filtering using a one-of-a-kind cadmium zinc telluride (CZT) PET system – establishing its viability as a multimodal scanner and ability to perform QE filtering. We show the high Compton scattering probability in this CZT-based scanner with 44.2% of gammas undergoing a single scatter prior to absorption. Additionally, the overall system sensitivity as a standard PET scanner (11.29%), QE-PET scanner (6.81%), and Compton Camera (11.29%) is quantified. Further, we find a 23% decrease in the double Compton scatter (DCSc) frequency needed for QE filtering for each mm decrease in crystal resolution and an increase in mean absolute error (MAE) of their $\Delta\phi$s from 6.8° for 1 mm resolution to 9.5° , 12.2° , and 15.3° for 2, 4, and 8 mm resolution, respectively. These results reinforce the potential of CZT detectors to lead next generation PET systems taking full advantage of the QE information of positron annihilation photons.

Index Terms—

PET Imaging; Quantum Entanglement; Prompt Gamma Imaging; GATE; Simulation Study

I. Introduction

Positron emission tomography (PET) is both a common, clinical medical imaging modality and an active area of research wherein the aim is to capture the distribution of an introduced, positron-emitting radiotracer within the imaging target [1], [2]. PET leverages the back-to-back, monoenergetic (~511 keV, typically) dual-gamma emission from positron-electron annihilation interactions to form lines of response (LOR) used in reconstruction. These

* sabbasza@ucsc.edu .

This work did not involve human subjects or animals in its research.

independently detected annihilation photons are paired in coincidence to form LORs based on sensitive energy and timing windows. This coincidence pairing process, however, is imperfect. “True” coincidences refer to the accurate pairings of gammas which both: originated from the same annihilation event and whose paths were not scattered. Incorrectly paired gammas which did not originated from the same annihilation event are referred to as “randoms,” typically incurred from finite-width coincidence timing windows. When one or both gammas scatter internally in the imaging target, their resulting LOR no longer captures the annihilation location information – such coincidences are called “scatters.” In Fig. 1, we provide visual representations of true, random, and scatter coincidences. Random and scatter coincidences result in false LORs which reduce the overall signal to noise ratio and degrade reconstructed image quality.

While the most widely used radiotracer in PET imaging is 2-[fluorine-18]fluoro-2-deoxy-D-glucose (^{18}F-FDG) due to its specificity for detection of cancerous lesions [3], unique radiotracers suit a variety of alternate and overlapping PET imaging tasks [4]–[10]. Some of these radiotracers, such as ^{89}Zr, have a prompt gamma decay in addition to the typical positron decay [9]–[11]. This prompt gamma can cause issues for coincidence pairing (and thus LOR definition) under certain conditions. For prompt gammas in the same energy window of the 511 keV annihilation photons or for those which can scatter into it, a false LOR can be generated between one annihilation photon and the prompt gamma [4], [12]. Secondly, for prompt gammas with higher energy, a false LOR can also be generated if the prompt gamma scatters into 511 keV window prior to detection [11]. Lastly, it is possible for prompt gammas in excess of 1022 keV to undergo pair production, which can result in additional 511 keV annihilation photons from secondary positrons [11]. Each of these eventualities essentially introduces a new source of randoms.

Despite this drawback, radiotracers with prompt gamma emissions afford the ability to pinpoint radiotracer location in a way that PET currently cannot. LORs capture information on the location of the annihilation interactions and not necessarily the location of the radiotracer which generated the positron. Depending on its energy and the medium, positron range can vary widely between radiotracers and between emissions from the same radiotracer. For example, ^{18}F has a mean positron range of 0.6 mm [11] while ^{60}Cu has a mean positron range of 21.0 mm [13]. Greater positron ranges can cause blurring of the target radiotracer distribution and have a negative effect on the attainable spatial resolution. Additionally, if the positron range is sufficiently great, artifacts such as “ghost uptakes” can occur if the positron annihilates outside the target organ [11]. Prompt gammas, on the other hand, are produced directly by radiotracer decay and are not affected by range effects. By using Compton kinematics to create a cone of response from prompt gamma interactions, the true location of the radiotracer can be found [13]. This information can be used in conjunction with the annihilation LOR to further increase radiotracer localization accuracy for radioisotopes with short delays between positron and prompt gamma emissions. Additionally, multi-isotope studies wherein prompt gamma ray signals are used to classify multiplexed annihilation gamma ray coincidence signals stand as a clear focus area [14]–[16]. Finally, for dual-emission isotopes, an opportunity for simultaneous, multi-modal imaging is available with PET-mode from positron emissions and Compton camera-mode for prompt gay emissions, enhancing imaging sensitivity should the signal be separable.

To maximize the benefits of prompt gamma radiotracers, our group proposes utilizing the concept of quantum entanglement filtering to combat the elevated random coincidence rate between prompt and annihilation gammas.

Quantum entanglement for imaging applications has been an area of study for several decades, with optical photons and x-ray photons utilizing entangled correlations [17]–[22]. The potential application of the complex positronium physics to medical imaging is vast [23]. While the physics of annihilation-based entanglement is well studied and the use of quantum entanglement properties in PET has been discussed in theory by many groups, there is limited experimental data available. Additionally, there are contradictory studies and reports regarding specific limitations of entanglement, so there is a need for continued work both theoretically and experimentally [24]–[32].

Wheeler hypothesized that a bound system of an electron and positron with zero orbital momentum would result in annihilation photons with perpendicular polarization due to the conservation of angular momentum and parity [33]. Then, in the late 1940s, Pryce and Ward and Snyder et al. theorized that – according to the Klein-Nishina formula – when two photons are emitted from an annihilation event and both undergo Compton scattering, the scatter distributions will be correlated in the azimuthal angle because of their perpendicular polarizations [34], [35]. Whether pre-detection scattering (triple Compton scattering or intermediate Compton scattering) causes loss of entanglement (decoherence) is disputed, with contradicting studies demonstrating either retention of entanglement [24] or loss of entanglement [25], [36] – Sharma et al. elaborates on this puzzle [37]. A pre-print study offers an additional investigation into the impact of the angle of the intermediate Compton scatter and shows entanglement is largely retained for small intermediate scattering angles and diminished with this magnitude [38]. As such, quantum entanglement theoretically offers an opportunity based on Compton scatter measurements to filter the random coincidences (as these gammas are not entangled) and scatter coincidences (as these gammas may no longer be entangled).

To observe the quantum entanglement, double Compton scattering (DCSc) must occur: both coincidence gammas must undergo an initial Compton scatter followed by a secondary interaction to extract the scattering vectors. A diagram of this event is shown in Fig. 2. Here, $\theta_{1,2}$ are the polar scattering angles of the respective photons, and $\phi_{1,2}$ are the azimuthal scattering angle. In other terms, θ describes the Compton cone (rotation off of the z-axis) while ϕ describes the placement of the scatter vector around the cone (rotation in the x-y plane). In systems where the x, y, z-positions of the LOR and scattering vectors are directly accessible, such as with the system in this study, extraction of these angles is straightforward. As an illustrative, high-level example of how to compute these angles on a coincidence-by-coincidence basis: the z-axis is aligned along the LOR vector while the x- and y-axes may be defined in any way such that they form a complete Cartesian coordinate basis with $\hat{z}$. θ is computed as the rotation about $\hat{z}$, and ϕ is computed as the rotation about $\hat{y}$ – using the coordination system in Fig. 2. While the secondary interactions are explicitly restricted to photoelectric absorption (or at least to a summed 511 keV interaction energy) in some experimental studies [24], [28], [39] (perhaps due to the ease of energy gating these multiple-interaction events), a second Compton scattering event

is, in principle, a tenable alternative. For example, Moskal et al. have made polarization (non-QE) measurements of annihilation photon using the J-PET system wherein the second interaction type is unrestricted [29]. Regardless, we limit the relevant portion of our study to Compton-to-photoelectric absorption events as the additional complexity of reclaiming multi-Compton event chains is beyond the scope.

Eq. 1 is the DCSc differential cross-section of entangled photons given by

$$\frac{d^2\sigma_{double}}{d\Omega_1 d\Omega_2} = \frac{r_0^4}{16}(K_a(\theta_1,\theta_2) - K_b(\theta_1,\theta_2)cos(2\Delta\phi)), \tag{1}$$

where σ_{double} is the double Compton scattering cross section, $\Omega_{1,2}$ are solid angles and polar scattering angles for the respective annihilation photons, r_0 is the electron radius, K_a and K_b are kinematic factors, $\theta_{1,2}$ are the polar scattering angles of the respective photons, and $\Delta\phi$ is the relative azimuthal scattering angle [24]. From Eq. (1), the scattering probability is influenced by the cosine term which in turn is dependent on the difference in azimuthal scattering angles, $\Delta\phi$. The enhancement ratio, R, is defined as the ratio of the scattering probabilities in the perpendicular ($\Delta\phi = 90°$), where scattering probability is maximized, and parallel directions ($\Delta\phi = 0°$), where scattering probability is minimized [35]. The enhancement ratio is derived from Eq. 1 in Eq. 2 for the case of both photons scattered through the same scattering angle,

$$R(\theta) = 1 + \frac{2sin^4\theta}{\gamma^2 - 2\gamma sin^2\theta};$$
$$\gamma = 2 - cos\theta + \frac{1}{2 - cos\theta}, \tag{2}$$

where θ is the polar scattering angle. Eq. 2 results in a value of R equal to 2.85 for entangled photons when both θ_1 and θ_2 are 81.7° [35]. This ratio was validated by Bohm and Aharonov, and a ratio of R=1.63 was determined for mixed separable (non-entangled) states of annihilation photons [40]. This ratio has previously been used to verify entangled and non-entangled states in simulation results [24], [34], [35], [40].

Thus, by computing the $\Delta\phi$ for each detected coincidence, we can estimate and minimize the contribution of random and scatter coincidences in positron-only PET. Importantly, it also enables the ability to filter the random prompt-annihilation coincidences when using a radiotracer with prompt gamma emissions based on the same metric – as prompt gammas are not subject to the QE annihilation physics. By leveraging the $\Delta\phi$ information obtained from DCSc photons, we gain the capability to effectively filter out false LORs, thereby enhancing the accuracy of the reconstruction, regardless of prompt or annihilation origin. To specify the implementation and limitations of such a technique, filtering cannot be performed on an event-by-event basis. While annihilation photons pairs are always linearly orthogonal in polarization, random coincidences may coincidentally have orthogonal polarization and thus exhibit the same azimuthal scattering kinematics. Instead,

the relative contribution of background (randoms and scatters) can be statistically estimated based on the true coincidence bias for perpendicular scattering. Watts et al. demonstrated a simple image-based solution wherein images formed from coincidences with relatively higher true rate ($\Delta\phi$ near 90°) and relatively lower true rates ($\Delta\phi$ near 0°) are scaled – based on simulation-extracted system-based true and scatter rate parameters – and subtracted [24].

Recent work has focused on experimentally verifying the polarization of annihilation photons in simulation. Ivashikin et al. experimentally studied the entanglement of photon pairs using Compton polarimeters comprised of sodium iodide counters, a plastic scatterer, and a gadolinium-aluminum-gallium garnet (GAGG) scintillator acting as an intermediate scatterer and found agreement theoretical results for entanglement of annihilation photons [25]. Parashari et al. studied five detector configurations using GAGG or lutetium-yttrium oxyorthosilicate scintillators to measure the angular correlations of annihilation photons [39], [41]. Watts et al incorporated linear polarization caused by entanglement in a GEANT4 simulation, then used a demonstrator apparatus made of cadmium zinc telluride (CZT) to experimentally confirm the simulated results [24].

The work of Watts et al. is especially relevant as their experimental CZT system constitutes a pixel-based segmented anode design [24], not too dissimilar to the anode-cathode cross-strip CZT system of this study. Their PET detector system comprised of two 10×10×10 mm^3 CZT crystals with a 11×11 array of segmented anodes forming 0.8×0.8 mm^2 anode pixels capable of depth information extraction from anode drift time measurements. They performed two experiments with this system. The first was a measurement of the $\Delta\phi$ distribution of a 170 kBq ^{22}Na source with 87 mm detector spacing to compare against simulated physics. The second was an investigation of entanglement loss by scattering induced by placing one detector 33° off axis with nylon scattering medium shielding the source. In both cases, good agreement was found between the simulated and experimental set-ups with high enhancement ratio demonstrated in the first and loss of entanglement in the limited-angle test. Most notably for this work, however, was their development of a QE-GEANT4 model expanding the Livermore polarized Compton scattering physics package to include the QE-based polarization and decoherent scattering [42], [43].

In this work, we will demonstrate via simulation the sensitivity of a novel PET system for such quantum entanglement filtering regarding annihilation and prompt gammas. We will also showcase the need for fine crystal resolution, i.e., the impact of imprecise gamma interaction location, with varied location binning. We will simulate a dual-panel PET system comprised of 2 opposite-facing panels of CZT detectors and data acquisition electronics that is currently under construction in our lab [44], [45]. One panel accommodates 15 rows of CZT modules (4×4×1cm^3). Each module consists of two CZT crystals (4×4×0.5 cm^3). Flexible circuits with gold stud bonding enable tight stacking of the CZT crystals with high packing fraction. Utilizing a cross-strip design, each CZT crystal has 39 anodes with a 1 mm pitch and 8 cathodes with a 5 mm pitch for a total of 47 channels. This design can achieve an x-y gamma interaction resolution of 1×2.5 mm via charge sharing information and sub-millimeter z-resolution with the use of cathode-to-anode ratio [46]. With this system design, we have shown accurate Compton scatter event recovery with an average polar angular resolution of 0.67° for 1×1×1 mm interaction resolution and 2.65° for 1×3×1 mm

interaction resolution [47], [48]. We have implemented this work in simulation due to the need for accurate positioning.

The system incorporates RENA boards based on the RENA ASIC, which provide precise event energy and time measurements. To facilitate data transmission, a 30:1 fan-in board connects multiple RENA boards to the PicoZed 7010/7020 board, with data fan-out achieved through a 1 GHz Ethernet cable connected to the small form-factor pluggable (SFP) connector and White Rabbit switch. With a maximum data transmission capability of 6.6 Gbps, the PicoZed board is linked to a dedicated DAQ computer. This high-bandwidth, custom-made modular design allows for scalability, enabling the system to be easily expanded by adding more boards to accommodate a variety of field of view sizes.

II. Methods

In this study, we investigate the efficacy of QE filtering through a series of simulated imaging studies using GATE [49], a GEANT4-based medical imaging simulation toolkit. The objectives of the investigation are four-fold. First, we assess the frequency of multiple interaction photon events (MIPEs) occurring throughout the lifetime of a photon in our simulated system to breakdown the inherent tendency of Compton scatter events. Second, we determine the sensitivity for different photon interaction event groups, specifically focusing on dual- prompt gamma and positron emitting radiotracers, to quantify the overall system sensitivity with and without prompt gamma inclusion. Third, we explore the impact of polarization and quantum entanglement physics on annihilation pair scattering distributions by analyzing the $\Delta\phi$ distributions achieved with different physics constructors – this method is primarily to demonstrate the capability of QE simulations in GATE. Finally, we examine the change in the quantity of Double-Compton and Single-Compton (DCSc) events and the accuracy of $\Delta\phi$ computations for four crystal bin sizes: 1 mm, 2 mm, 4 mm, and 8 mm. The following sections outline the exact procedures followed for each of these objectives.

A. System geometry in GATE

The dual-panel PET system geometry is replicated within GATE and is shown in Fig. 3. The detector face is 15×20 cm^2, and the panel faces are separated by 20 cm. Each panel has one-hundred fifty 40 × 5× 40mm^3 CZT crystals placed in a 5×30 array. The edge-on configuration utilizes 4 cm of crystal thickness. This, in addition to the high effective atomic number of CZT, allows the system to be an ideal candidate to detect a significant number of Compton scattering events.

B. Simulation parameters

Two sources are defined: the first is a dual emitter of prompt gammas and annihilation gamma-pairs (constructed using the “pPs” extended source model in GATE, wherein two-photon emission from parapositronium decay is modelled with the optional prompt gamma emission enabled) used to investigate the MIPE and event group distributions, and another pure positron source for the quantum entanglement studies. Both are 30 μCi point sources with 0.5 mm radius and are centered in the system’s FOV. The dual source

emulated a simplified ^{89}Zr isotope with 100% of decays yielding back-to-back 511 keV annihilation photons and a 909 keV prompt gamma simultaneously. The pure positron source yielded only positrons with each decay. The standard *emlivermore_polar* physics list for electromagnetic physics is activated for MIPEs and event group sensitivity studies. The physics list used in quantum entanglement study is discussed in the next section. Each simulation is run for 30 s with the same random seed (2023) using the Mersenne Twister random number engine. No blurring in time, space, or energy was applied to focus on raw, system agnostic (geometry aside) performance.

C. Activating quantum entanglement physics in GATE

Standard physics lists in GEANT4 [50] which enable the electromagnetic processes for simulation of the detection and generation of positron annihilation photons do not contain the quantum entanglement physics required for this study. Contributions from Watts et al. [24], however, released in GEANT4 11.0 have recently incorporated such optional physics into the Livermore polarized Compton model utilized by the physics constructor *emlivermore_polar*, an inherited constructor of *emlivermore* which enables gamma polarization physics allowing us to observe non-uniform distributions of polarized annihilation gammas in Compton scattering events. While the quantum entangle physics is toggleable via a UI command in GEANT4, GATE currently does not have such a feature out of the box.

However, an edit to underlying GEANT4 *emlivermore_polar* physics constructor can enable quantum entanglement physics in GEANT4 whenever this constructor is used, which is passed on to GATE calls. With the simplicity of the edit, it is summarized here:

Within the GEANT4 source file G4EMLivermorePolarizedPhysics.cc, after “param->SetEnablePolarisation(true);” in line 42, add “param->SetQuantumEntanglement(true);”. The user then needs to *make* and *make install* the edit.

Therefore, the quantum entanglement testing GATE simulations are conducted separately for the following physics lists: *emlivermore*, *emlivermore_polar*, and Quantum Entanglement enabled *emlivermore_polar*.

D. Data processing

In all studies, the GATE hits file output is used, which contains the true information about the location, time, energy, and physical process of each particle interaction which occurred during the simulations. In the MIPEs study, we extract from the hits file the number of Compton scatters each 511 keV photon undergoes before it is absorbed in the system via photoelectric absorption. Here, the ground truth information allows for observation of the underlying physics. In the event group sensitivity study, we compute the frequency of each relevant combination of possible annihilation photon and prompt gamma photon interactions. For example, both annihilation photons undergoing photoelectric absorption (with no prior scattering) and the prompt gamma Compton scattering is one possible event group.

For the quantum entanglement studies, the hits file is searched for DCSc annihilation photon pairs, recording the coordinates of each annihilation gammas' initial scatter and subsequent absorption. A separate script then computes the polar and azimuthal scattering angles for each DCSc to generate the $\Delta\phi$ distribution. For inspecting changes incurred from crystal bin sizing, the hit coordinates are uniformly binned in increments of 1, 2, 4, and 8 mm in x, y, and z prior to any further processing. Thus, five data sets are available, one ground truth and four of the varied crystal resolution.

III. Results

A. Multiple Interaction Photon Events

In the MIPEs simulation study, we are interested in the distribution in the frequency of Compton scatter interactions preceding a photoelectric absorption by the 511 keV annihilation photons within the detector. Table I summarizes these results. Findings in a previous study on a dedicated CZT system report similar results [48]. There is a high Compton scattering probability for photons entering the detector with 85.5% of photons undergoing at least one Compton scatter before being absorbed by the system. We bring attention to the 1C, 1P column which describes the DCSc event chain that is used to observe quantum entangled annihilation photons. This interaction chain constitutes 44.2 % of total event-chains detected and demonstrates that DCSc events represent more than triple the direct photoelectric absorption events which occurs at 14.5% for CZT. This high frequency of DCSc events confirms the capability in observing quantum entanglement of annihilation photons in our dual-panel system and demonstrates that sensitivity to DCSc events is in fact greater than that of the generally preferred 0C, 1P interaction. Further, with Compton kinematic calculations and sufficient energy and timing windows, successive Compton scatter locations may also be utilized in forming DCSc events, greater expanding system sensitivity. It must be noted, however, that the DCSc event coincidences do not represent the final data set for reconstruction – this set must first be filtered to extract only those coincidences which are believed to be entangled, reducing the final coincidence count rate by a margin dependent on scattering angle thresholds.

B. Dual Panel event group detection sensitivity

In the event group sensitivity study, the groups of interest are those which contribute to system operation as a stand-alone PET detector, a stand-alone Compton camera, or as a dual system. Each group contains three photons generated from a single radiotracer molecule: two annihilation gammas (originating from the positron emission) and one prompt gamma. We classify photons by their primary interaction when first entering the detector volume. "Photoelectric" represents the photon being fully absorbed by the detector with no MIPEs. "Compton" represents the photon first undergoing Compton scattering before subsequently being absorbed via photoelectric absorption.

We present results of the overall sensitivity of our dual-panel CZT system in Table II. The overall sensitivity of the PET detector is the summation of Group 1 through 6, which results in a sensitivity of 11.29%. Groups 3 and 4 represent the interactions that will benefit from quantum entanglement filtering. These two groups account for 6.81% of detected decays

which makes up a large part of the PET sensitivity and allows for the elimination of randoms for over half of possible LORs. Additionally, there is potential to use the dual-panel system as a Compton camera to reduce positron range effects and localize the decay location more accurately. Groups 1, 4, 5, and 7 have useful prompt gamma interactions, accounting for 10.05% of decays. Decays in Group 7 are of particular interest as these decays do not contain a traditional LOR for the PET system, but the decay location information can be found via a cone of response for the prompt gamma, increasing the sensitivity by a possible 8.92 percentage-points.

C. Quantum Entanglement measurement in positron emission tomography

The objective of this portion off the study is to demonstrate the availability of simulated QE physics in GATE by presenting the DCSc frequency when QE is enabled. We have chosen to reproduce the GEANT4 demonstration of the DCSc curves obtained with different physics enabled shown by Fig. 2 in Watts et al. [24] in GATE (using our system) to this end. To facilitate this comparison, the simulations were conducted using identical parameters while employing different physics lists. Fig. 4 provides a comprehensive illustration of the impact of incorporating the QE and polarization processes on the coincidence count rate. This data was filtered with respect to polar scatter angles, θ, limited to a range of 70° to 110°. The azimuthal scattering angles $\Delta\phi$ are binned into 10° bins.

In Fig. 4, the x-axis represents the variable $\Delta\phi$, the difference in azimuthal scattering angle, while the y-axis denotes the normalized coincidence count rate. Normalization is based on the mean count rate at angles $\Delta\phi = 0°$ and ±180° from the *emLivermore* physics constructor simulation (green line, star). Line widths represent the standard deviation statistical uncertainties derived from the simulated events' yield in each bin. Here, the normalized coincidence count rate is the same as the enhancement ratio described previously in Eq. (2).

Without polarization physics or QE enabled, *emLivermore* library (green line, star), an enhancement ratio of R=1.013 ± 0.002 is achieved and is expected. Adding polarization to the simulation physics with the *emLivermore_Polar* constructor (red line, square) yields a greater enhancement ratio of R=1.453 ± 0.010. Incorporating polarization and QE with the *emLivermore_Polar+QE* constructor (blue line, triangle) results in the largest enhancement ratio of R=2.035 ± 0.020.

Similarly, Watts et al. demonstrated a strong $\Delta\phi$ modulation, achieving a QE enhancement ratio 1.85 ± 0.04 with the same polar scattering filter [24]. Their curves corresponding to non-entangled but polarized and non-polarized photons are similarly framed, respectively. The difference in magnitude (enhancement ratio), being lower for their experimental and simulated analysis, is attributable to the additional energy and spatial binning they performed for this test.

These curves demonstrate the clear impact of polarization and QE physics on azimuthal scattering difference distributions for annihilation gammas. Of all annihilations, 0.03% resulted in DCSc events (both gammas undergoing 1C, 1P events); and of detected coincidences with full energy deposition (XC, 1P), 12.82% resulted in DCSc events. These

events must further be filtered by polar and azimuthal scattering angle difference, however. Limiting θ to a range of 70° to 110°, 9.78% of these DCSc coincidence survive (or 1.25% of XC, 1P coincidences).

It is important to note that the DCSc events are defined as dual 1C, 1P events. The results presented in Table II which refer to "Compton" are for XC, 1P events (with X > 0).

D. Impact of crystal resolution on DCSs frequency and Δϕ accuracy

Thus far, the ground truth hit information has been used, specifically the interaction location coordinates. Using arbitrarily fine resolution in this regard provides utility in analyzing the underlying physics of scattering, MIPE frequency, and event group frequency independent of system performance. However, the precision needed in ascertaining scattering kinematics necessitates a more grounded look at the data. In this section, we present the result of the impact on crystal resolution (coordinate binning, more specifically) on QE filtering. No blurring in energy or time is considered here.

Foremost, two consequences emerge as the spatial bin size increased (1, 2, 4, and 8 mm): (1) the accuracy of the computed $\Delta\phi$ decreases, and (2) the quantity of DCSc decreases. These effects are summarized in Table III as the percent of surviving DCSc from no binning, the root mean squared error (RMSE), and the mean squared error (MAE). The surviving DCSc decreases by ~23% for each mm increase in binning. System sensitivity to DCSc is directly proportional to the crystal resolution. This change can be attributed to the post-scatter range of the gamma being less than the binning size more frequency as bin size increases. For example, a gamma which travels 1.2 mm between its Compton and photoelectric absorption events will contribute to a DCSc with 1 mm binning but not necessarily for 2 mm (or 4 or 8 mm) binning as both events may occur at the same (functional) location. Larger bin sizes also means less angular resolution is available for computing θ and $\Delta\phi$. As such, we observe RMSE and MAE increase with bin size. The anomalously low RMSE for 8 mm binning is likely attributed to the surviving scattering vectors aligning with crystal array more so than for the previous steps.

Both impacts are visualized in Fig. 5 where each plot contains the data for one binning set. Here, the x-axis is the true $\Delta\phi$ acquired with no coordinate binning, and the y-axis the computed $\Delta\phi$ when binning is considered. Each point represents one DCSc event. The mean trend-line and standard deviation is shown for 10° steps. As the bin size increases, we can observe the density of each plot decreasing and the standard deviation increasing. Further, we observe that the error rate is constant across $|\Delta\phi|$, not biased towards certain angles as bin size changes.

In Fig. 6, we inspect the degrading accuracy of the $\Delta\phi$ with bin size. In both plots, we are considering the absolute error in computation: $|\Delta\phi_{true} - \Delta\phi_{binned}|$. The box and whisker plots in Fig. 6(a) provide a summary of the error distribution for each crystal bin size. From this plot, we can see the median error increasing with bin size as well as the spread in error. In Fig. 6(b), we look at the cumulative error frequency – a point at (20, 0.4) indicates 40% of the data has an error of 20° or less. We can see in more detail the small bin sizes result in

lower overall error with 1 mm binning resulting in an error of 10° or less ~80% of the time compared to 2 mm yielding ~15°, 4 mm 20°, and 8 mm 25° at that same frequency.

IV. Discussion

This paper presents an innovative approach based on QE filtering to leverage the prompt gamma decays of novel radiotracers in our CZT-based PET system. Utilizing the prompt gamma decay emitted by the radiotracer offers the potential to enhance the system's spatial resolution by mitigating the effects caused by positron range but comes with the drawback of confounding coincidence pairing with energy window overlap. QE filtering may aid in this endeavor (particularly Groups 3 and 4) by reducing the increased background signal dual emission confers, though further testing is needed.

The CZT detector, characterized by its unique edge-on configuration and high atomic number, exhibits a high probability of Compton scattering for incoming photons. In addition, the cross-strip design affords high spatial resolution of crystal interaction events. Through simulations, we demonstrate that 1C, 1P event chains (half of a DCSc) account for 44.227% of detected event chains, and 12.82% of full energy deposition coincidences are DCSc, confirming the feasibility of observing quantum entanglement with the dual-panel system.

Complications with extracting DCSc and then computing $\Delta\phi$ also strongly favor systems with fine crystal resolutions. We observed an ~23% decrease in DCSc frequency for each mm increase in bin size, dampening the already lower DCSc rate as compared to normal coincidences. We also found the 80% cumulative error frequency increases by 5° for each doubling of bin size. These errors impact the efficacy of $\Delta\phi$ thresholding and the overall accuracy of true coincidence filtering. The presented system achieves a hit resolution of 1×2.5×<1 mm. While this performance is best captured by the 1 mm hit binned data, the anisotropic resolution may bias the frequency and magnitude of errors for certain angles. However, we expect the benefits of the greater resolution to outweigh this potential given these results.

Simulations of our dual-panel system show a sensitivity of 11.29%, with up to 6.81% of coincidences eligible for quantum filtering, leading to the reduction of random and scatter events for over half of the detected LORs. By incorporating the radiotracer with prompt gamma decay, an additional 8.92% sensitivity could potentially be achieved by utilizing the cone of response for prompt gamma when LORs from annihilation photons are not available.

These results also highlight the CZT system's potential for multi-isotope imaging through hybrid operation as a standard PET and Compton Camera. The ability to seamlessly operate in both modes enhances the system's sensitivity and improves the spatial resolution for imaging radioisotopes with long half-lives, such as 89Zr. By utilizing GATE simulations of our dual-panel CZT system, we have confirmed previous findings regarding the system's capability to regarding MIPE frequency, demonstrated the gained sensitivity from using a prompt gamma emitting radioisotope, and shown the degree to which QE filtering can both mitigate the randoms induced by the prompt gammas and enhance the true coincidence rate.

It is important to remember that the data sets used in this analysis are based on *a priori* knowledge for MIPE grouping, coincidence pairing, and DCSc coincidence pairing. As such, these finding represent the best-case scenario for increases in system sensitivity and error rates for $\Delta\phi$ with the given system – though we have demonstrated promising results for Compton event recovery [45], [48]. While the means for distinguishing between prompt and annihilation gamma ray signals may be feasible based on these findings, development of such a technique constitutes future work. We have demonstrated event-by-event discrimination based purely on $\Delta\phi$ filtering yields poor but better than nothing classification results, as expected [26]. Despite this, Kim et al. has recently demonstrated an in increase to signal-to-noise ratio in reconstructed images based solely on $\Delta\phi$ filtered coincidence data [28]. However, filtering coincidence data on θ and $\Delta\phi$ has severe implications for overall system sensitivity. Watts et al.'s demonstrational approach instead corrects the reconstructed images based on QE-calibration data and estimated true and non-true signals from near-90° $\Delta\phi$ coincidences and near-0° $\Delta\phi$ coincidences [24]. Such an approach is constrained by the feasibility and efficacy of QE-calibration. Greater research is needed in this aspect of QE-PET to improve these early attempts of leveraging QE-based information for reconstruction.

V. Conclusion

Overall, this study demonstrates that QE filtering of gamma interactions holds promise as a powerful tool for optimizing the true coincident rate in positron-only PET and enabling prompt gamma identification in dual-imaging applications. By enabling the selection of annihilation-origin, non-scattered gamma pairs, this technique addresses some of the major hurdles encountered when incorporating prompt gamma radiotracers into PET studies. However, it is essential to acknowledge the hurdles of QE filtering, itself. While this technique is theoretically system-agnostic (in that as long as Compton kinematics are commutable, QE filtering can be done), in reality, it demands an imaging system with sufficient hit resolution to effectively capitalize up on it. While overall system sensitivity conditionally expands, the θ and $\Delta\phi$ gamma thresholding has a significant impact on coincident count rate, even when only inspecting a true coincidence data set. The proposed CZT system, with its favorable sensitivity for the DCSc events (constituted of dual 1C, 1P MIPEs) and the mm-resolution offered by the cross-strip design, proves crucial for accurate QE filtering. Future research should consider the impact of additional system loss factors, such as temporal resolution, energy resolution, and the accuracy of Compton kinematics on the reconstructed images. Addressing these factors will shed light on the practical feasibility and applicability of QE filtering in diverse imaging setups. In conclusion, the findings from this study underscore the potential of QE filtering as an enabler of dual prompt gamma and PET imaging. By leveraging its benefits while being mindful of its limitations and system requirements, we can enhance the capabilities of PET and potentially open new avenues for dual-imaging applications.

ACKNOWLEDGMENTS

All authors declare that they have no known conflicts of interest in terms of competing financial interests or personal relationships that could have an influence or are relevant to the work reported in this paper. The authors

acknowledge the support from the National Institute of Biomedical Imaging and Bioengineering of the National Institutes of Health under Award Numbers R01EB028091 and UG3EB034686.

REFERENCES

[1]. Alavi A, Werner TJ, Stępień EL, and Moskal P, "Unparalleled and revolutionary impact of PET imaging on research and day to day practice of medicine," Bio-Algorithms and Med-Systems, vol. 17, no. 4, pp. 203–212, 2021.

[2]. Unterrainer M et al. , "Recent advances of PET imaging in clinical radiation oncology," Radiation Oncology, vol. 15, pp. 1–15, 2020.

[3]. Miele E et al. , "Positron emission tomography (PET) radiotracers in oncology–utility of 18F-Fluoro-deoxy-glucose (FDG)-PET in the management of patients with non-small-cell lung cancer (NSCLC)," Journal of Experimental & Clinical Cancer Research, vol. 27, no. 1, pp. 1–10, 2008.

[4]. Lubberink M, Schneider H, Bergström M, and Lundqvist H, "Quantitative imaging and correction for cascade gamma radiation of 76Br with 2D and 3D PET," Physics in Medicine & Biology, vol. 47, no. 19, p. 3519, 2002. [PubMed: 12408479]

[5]. Freudenberg LS, Jentzen W, Stahl A, Bockisch A, and Rosenbaum-Krumme SJ, "Clinical applications of 124 I-PET/CT in patients with differentiated thyroid cancer," European journal of nuclear medicine and molecular imaging, vol. 38, pp. 48–56, 2011.

[6]. Banerjee SR and Pomper MG, "Clinical applications of Gallium-68," Applied Radiation and Isotopes, vol. 76, pp. 2–13, 2013. [PubMed: 23522791]

[7]. Mishra A et al. , "Gallium-68–labeled peptide PET quantifies tumor exposure of PD-L1 therapeutics," Clinical Cancer Research, vol. 29, no. 3, pp. 581–591, 2023. [PubMed: 36449662]

[8]. Al-Nahhas A, Win Z, Szyszko T, Singh A, Nanni C, Fanti S, and Rubello D, "Gallium-68 PET: a new frontier in receptor cancer imaging," Anticancer research, vol. 27, no. 6B, pp. 4087–4094, 2007. [PubMed: 18225576]

[9]. Natarajan A et al. , "Preclinical evaluation of 89Zr-panitumumab for biology-guided radiation therapy," International Journal of Radiation Oncology* Biology* Physics, 2023.

[10]. Lee YJ et al. , "89Zr-panitumumab combined with 18F-FDG PET improves detection and staging of head and neck squamous cell carcinoma," Clinical Cancer Research, vol. 28, no. 20, pp. 4425–4434, 2022. [PubMed: 35929985]

[11]. Conti M and Eriksson L, "Physics of pure and non-pure positron emitters for PET: a review and a discussion," EJNMMI physics, vol. 3, pp. 1–17, 2016. [PubMed: 26782039]

[12]. Andreyev A and Celler A, "Dual-isotope PET using positron-gamma emitters," Physics in Medicine & Biology, vol. 56, no. 14, p. 4539, 2011. [PubMed: 21725143]

[13]. Beekman FJ, Kamphuis C, Koustoulidou S, Ramakers RM, and Goorden MC, "Positron range-free and multi-isotope tomography of positron emitters," Physics in Medicine & Biology, vol. 66, no. 6, p. 065011, 2021. [PubMed: 33578400]

[14]. Beyene EY et al. , "Exploration of simultaneous dual-isotope imaging with multi-photon modular J-PET scanner," Bio-Algorithms and Med-Systems, vol. 19, no. 1, pp. 101–108, 2023.

[15]. Pratt EC et al. , "Simultaneous quantitative imaging of two PET radiotracers via the detection of positron–electron annihilation and prompt gamma emissions," Nature Biomedical Engineering, vol. 7, no. 78, pp. 1028–1039, 2023.

[16]. Fukuchi T, Okauchi T, Shigeta M, Yamamoto S, Watanabe Y, and Enomoto S, "Positron Emission Tomography with additional γ-ray detectors for multiple-tracer imaging," Medical Physics, vol. 44, no. 6, pp. 2257–2266, 2017. [PubMed: 28168704]

[17]. Pittman TB, Shih YH, Strekalov DV, and Sergienko AV, "Optical imaging by means of two-photon quantum entanglement," Physical Review A, vol. 52, no. 5, p. R3429, 1995.

[18]. Brida G, Genovese M, and Ruo Berchera I, "Experimental realization of sub-shot-noise quantum imaging," Nature Photonics, vol. 4, no. 4, pp. 227–230, 2010.

[19]. Genovese M, "Real applications of quantum imaging," Journal of Optics, vol. 18, no. 7, p. 073002, 2016.

[20]. Sofer S, Strizhevsky E, Schori A, Tamasaku K, and Shwartz S, "Quantum enhanced X-ray detection," Physical Review X, vol. 9, no. 3, p. 031033, 2019.

[21]. Kuznetsova E and Kocharovskaya O, “Quantum optics with X-rays,” Nature Photonics, vol. 11, no. 11, pp. 685–686, 2017.

[22]. Adams BW et al. , “X-ray quantum optics,” Journal of modern optics, vol. 60, no. 1, pp. 2–21, 2013.

[23]. Bass SD, Mariazzi S, Moskal P, and Stepien E, “Colloquium: Positronium physics and biomedical applications,” Rev. Mod. Phys, vol. 95, p. 021002, May 2023.

[24]. Watts DP et al. , “Photon quantum entanglement in the MeV regime and its application in PET imaging,” Nature Communications, vol. 12, no. 1, p. 2646, 2021.

[25]. Ivashkin A et al. , “Testing entanglement of annihilation photons,” Scientific Reports, vol. 13, no. 1, pp. 1–11, 2023. [PubMed: 36593249]

[26]. Romanchek G, Shopp G, and Abbaszadeh S, “Application of quantum entanglement induced polarization for dual-positron and prompt gamma imaging,” Bio-Algorithms and Med-Systems, vol. 19, no. 1, pp. 9–16, 2023. [PubMed: 39081536]

[27]. Parashari S et al. , “Optimization of detector modules for measuring gamma-ray polarization in Positron Emission Tomography,” Nuclear Instruments and Methods in Physics Research Section A: Accelerators, Spectrometers, Detectors and Associated Equipment, vol. 1014, p. 167186, 2022.

[28]. Kim D, Rachman AN, Taisei U, Uenomachi M, Shimazoe K, and Takahashi H, “Background reduction in PET by double Compton scattering of quantum entangled annihilation photons,” Journal of Instrumentation, vol. 18, no. 7, p. P07007, 2023.

[29]. Moskal P, “Towards total-body modular PET for positronium and quantum entanglement imaging,” Proc. IEEE Nuclear Science Symposium and Medical Imaging Conference Proceedings, vol. 18, no. 7, pp. 1–4, 2018.

[30]. Moskal P et al. , “Feasibility studies of the polarization of photons beyond the optical wavelength regime with the J-PET detector,” The European Physical Journal C, vol. 87, pp. 1–9, 2018.

[31]. Hiesmayr BC and Moskal P, “Witnessing entanglement in Compton scattering processes via mutually unbiased bases,” Scientific reports, vol. 9, no. 1, pp. 1–14, 2019. [PubMed: 30626917]

[32]. Caradonna P, Reutens D, Takahashi T, Takeda S, and Vegh V, “Probing entanglement in Compton interactions,” Journal of Physics Communications, vol. 3, no. 10, p. 105005, 2019.

[33]. Wheeler JA, “Polyelectrons,” Annals of the New York Academy of Sciences, vol. 48, no. 3, pp. 219–238, 1946.

[34]. Pryce MHL and Ward JC, “Angular correlation effects with annihilation radiation,” Nature, vol. 160, no. 4065, pp. 435–435, 1947. [PubMed: 20265544]

[35]. Snyder HS, Pasternack S, and Hornbostel J, “Angular correlation of scattered annihilation radiation,” Physical Review, vol. 73, no. 5, p. 440, 1948.

[36]. Abdurashitov D et al. , “Setup of Compton polarimeters for measuring entangled annihilation photons,” Journal of Instrumentation, vol. 17, no. 3, p. P03010, 2022.

[37]. Sharma S, Kumar D, and Moskal P. f. t. J.-P. C., “Decoherence puzzle in measurements of photons originating from electron-positron annihilation,” Acta Phys. Pol. A, vol. 142, p. 428, 2022.

[38]. Bordes J, Brown JR, Watts DP, Bashkanov M, Newton R, and Zachariou N, “A first detailed study of the quantum decoherence of entangled gamma photons,” *ar*Xiv preprint, 2023.

[39]. Parashari S et al. , “Optimization of detector modules for measuring gamma-ray polarization in positron emission tomography,” Nuclear Instruments and Methods in Physics Research Section A: Accelerators, Spectrometers, Detectors and Associated Equipment, vol. 1040, p. 167186, 2022.

[40]. Bohm D and Aharonov Y, “Discussion of experimental proof for the paradox of Einstein, Rosen, and Podolsky,” Physical Review, vol. 108, no. 4, p. 1070, 1957.

[41]. Kožuljević AM, Bosnar D, Kuncic Z, Makek M, Parashari S, and Žugec P, “Study of multi-pixel scintillator detector configurations for measuring polarized gamma radiation,” Condensed Matter, vol. 6, no. 4, p. 43, 2021.

[42]. Cullen DE, Hubbell JH, , and Kissel L, “EPDL97: the evaluated photo data library97 version,” Lawrence Livermore National Lab.(LLNL), vol. 6-Rev. 5, no. UCLR-50400, 1997.

[43]. Perkins ST, Cullen DE, Chen MH, Rathkopf J, Scofield J, , and Hubbell JH, "Tables and graphs of atomic subshell and relaxation data derived from the llnl evaluated Atomic Data Library (EADL), Z= 1–100," Lawrence Livermore National Lab.(LLNL), vol. 30, no. UCLR-50400, 1991.

[44]. Enlow E, Diba M, Clayton J, Harris B, and Abbaszadeh S, "Impact of flexible circuit bonding and system integration on energy resolution of cross-strip CZT detectors," IEEE Transactions on Radiation and Plasma Medical Sciences, 2023.

[45]. Wang Y, Herbst R, and Abbaszadeh S, "Development and characterization of modular readout design for two-panel head-and-neck dedicated PET system based on CZT detectors," IEEE Transactions on Radiation and Plasma Medical Sciences, vol. 6, no. 5, pp. 517–521, 2021. [PubMed: 37711549]

[46]. Gu Y and Levin CS, "Study of electrode pattern design for a CZT-based PET detector," Physics in Medicine & Biology, vol. 59, no. 11, p. 2599, 2014. [PubMed: 24786208]

[47]. Yang S, Li M, Reed M, Hugg J, Chen H, and S. A, "Effect of CZT system characteristics on Compton scatter event recovery," IEEE transactions on radiation and plasma medical sciences, vol. 4, no. 1, pp. 91–97, 2019. [PubMed: 31922083]

[48]. Abbaszadeh S, Chinn G, and Levin CS, "Positioning true coincidences that undergo inter-and intra-crystal scatter for a sub-mm resolution cadmium zinc telluride-based PET system," Physics in Medicine & Biology, vol. 63, no. 2, p. 025012, 2018. [PubMed: 29131809]

[49]. Jan S et al. , "Gate: a simulation toolkit for PET and SPECT," Physics in Medicine & Biology, vol. 49, no. 19, p. 4543, 2004. [PubMed: 15552416]

[50]. Agostinelli S et al. , "Geant4—a simulation toolkit," Nuclear Instruments and Methods in Physics Research Section A: Accelerators, Spectrometers, Detectors and Associated Equipment, vol. 506, no. 3, pp. 250–303, 2003.

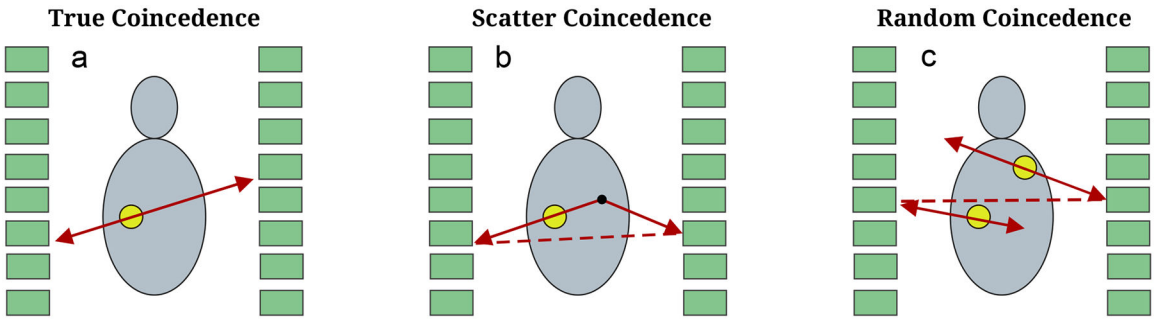

Fig. 1:

a) Shows the LOR of a true coincidence event where pairs of photons originating from the same positron are detected. b) Creates a false LOR in the dashed line where one of the pairs of photons is scattered off its true LOR. c) Two pairs of annihilation photons create a false LOR.

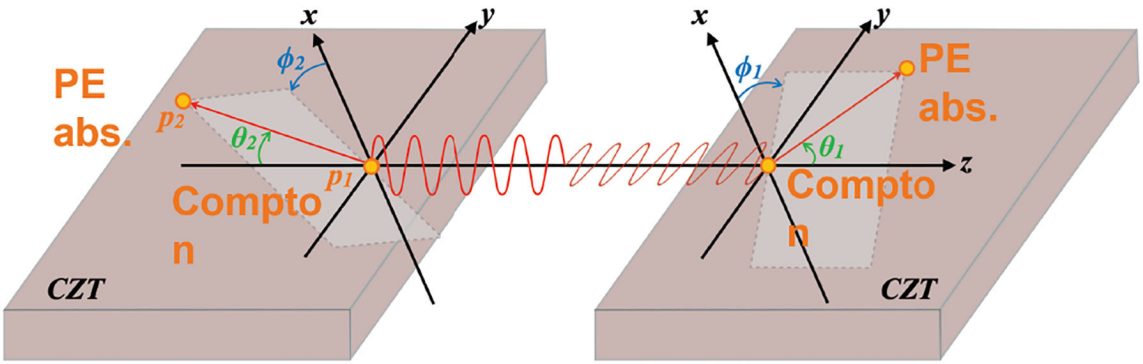

Fig. 2:

The z-axis is aligned with the LOR trajectory. θ is the classical polar scattering angle off the z-axis. ϕ is the azimuthal scattering angle in the x-y plane.

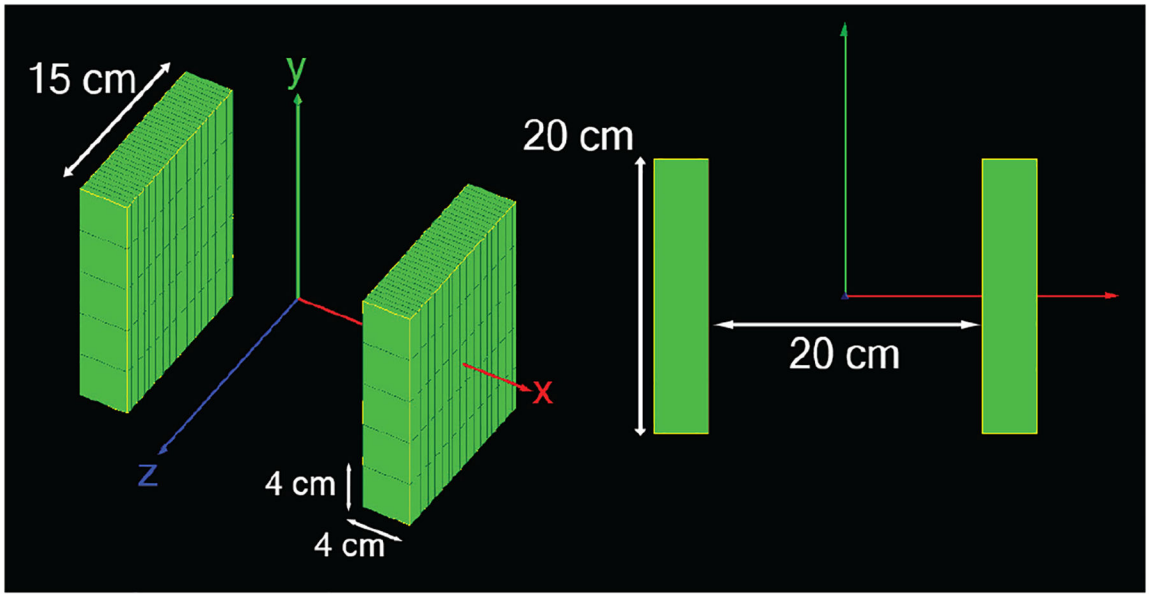

Fig. 3:

Left–Oblique view of dual-panel CZT scanner geometry visualized in GATE. Demonstrating the edge-on configuration of the scanner with the 4×4 cm^2 face of the CZT crystals oriented in the z-direction. Right–View along the z-axis to demonstrate the spacing between panels and the extent in the y-direction.

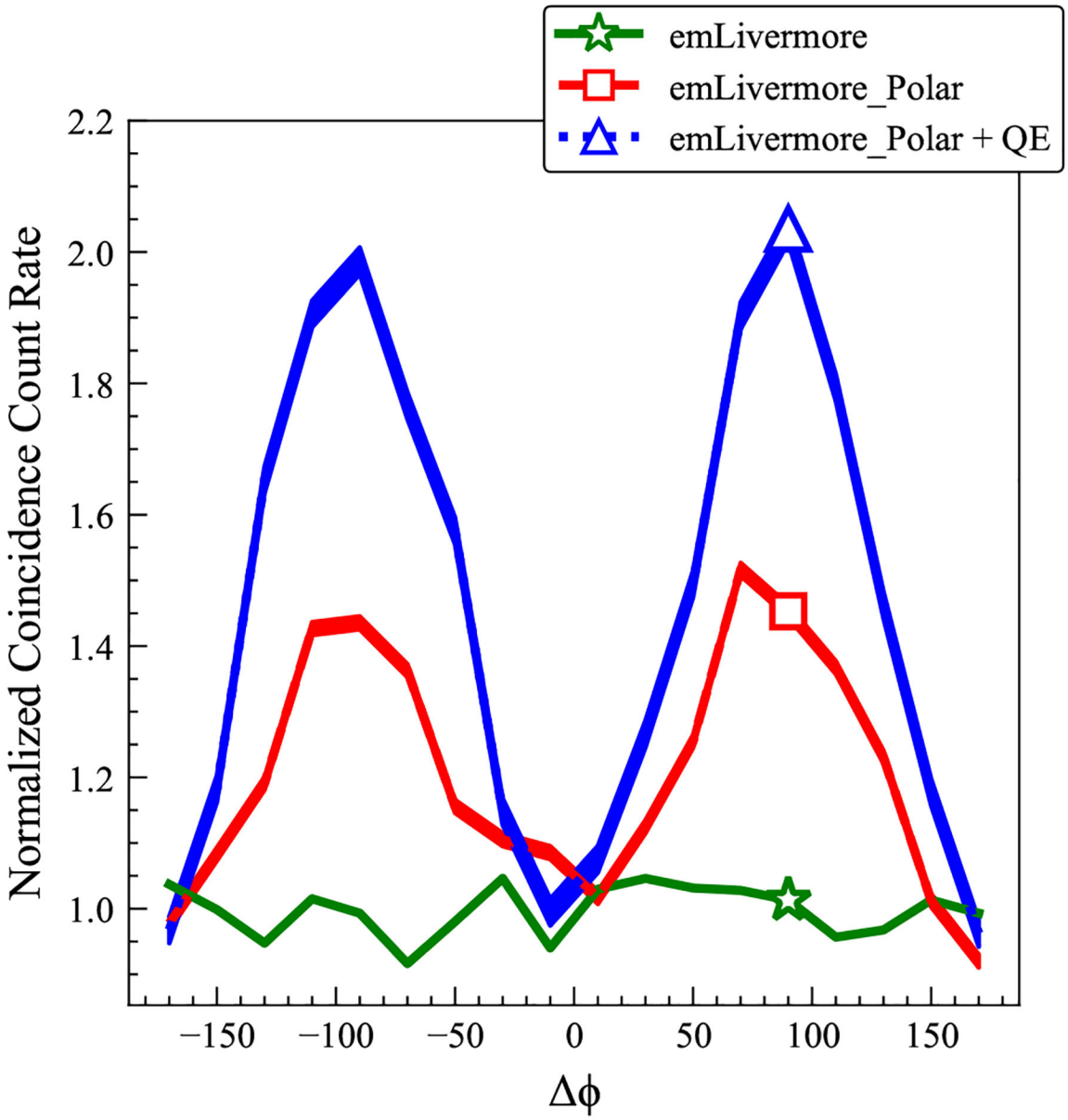

Fig. 4:

Comparison of simulated scattering frequency using different physics libraries and true DCSc. The plot displays three lines representing simulation results obtained using different libraries. The green line corresponds to the *emLivermore* library, the red line represents the *emLivermore_Polar* library, and the blue line illustrates the *emLivermore_Polar* library with the activation of the Quantum Entanglement (QE) process. These results are based on a perfect CZT detector, with infinite hit precision in time, energy, and space.

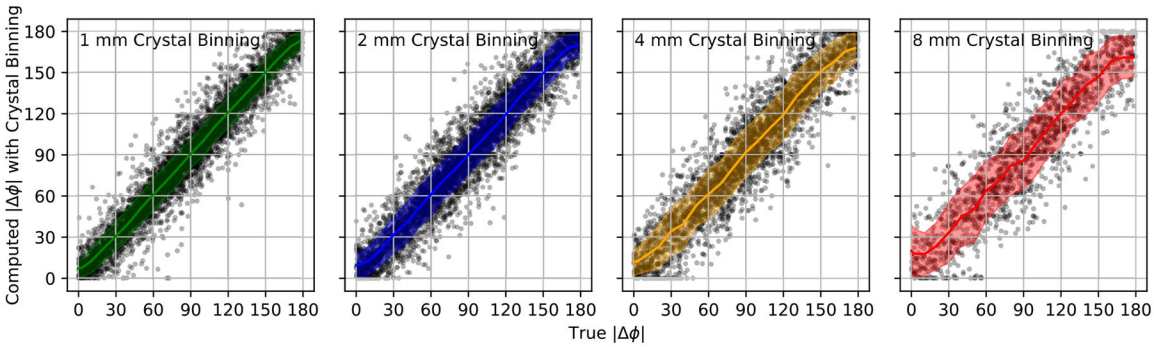

Fig. 5:

The computed $|\Delta\phi|$ with coordinate binning vs without coordinate binning. From left to right, the data than has been binned to 1 mm, 2 mm, 4 mm, and 8 mm. The number of data points change with each plot as DCSc with gamma ranges less than the bin size cannot have their scattering angles computed. The trend-line is the mean computed in 10° increments while the shaded area is the standard deviation.

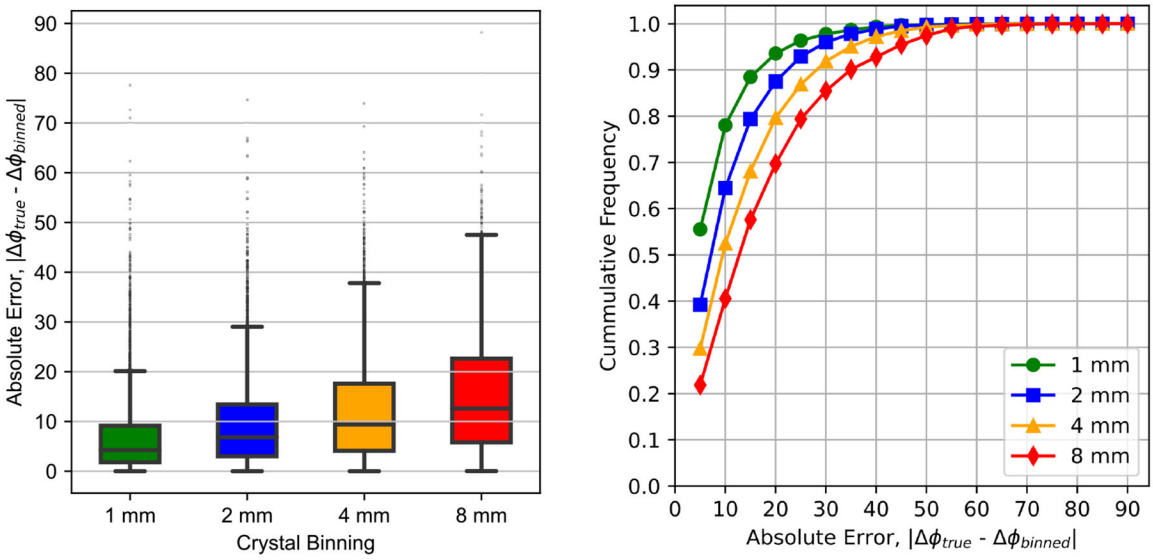

(a) Box and Whisker plots of error distributions

(b) Cumulative error frequency

Fig. 6:

Visualisation of the distribution of error rates for the given bin sizes: 1, 2, 4, and 8 mm. (a) The box plots and density curves for each bin size. (b) The cumulative error frequency for each bin size.

TABLE I:

Fractions of photons detected undergoing none or multiple Compton scattering interactions before being absorbed by the detector. Events shown under column headings describe the number of the event occurring throughout the photons lifetime followed by either C = Compton scattering or P = photoelectric absorption.

Total Events Detected	0C/1P	1C/1P	2C/1P	3C/1P	4C/1P	>4C
20,679,843	2,998,755	9,146,103	5,313,059	2,251,191	729,632	241,103
	14.5 %	44.2 %	25.7 %	10.9 %	3.5 %	1.2 %

TABLE II:

System sensitivity to types of interactions detected in the dual-PET system. Groups of events are defined by the first physical interactions a pair of annihilation photons and their associated prompt gamma encounter when entering the detector. Photons with Compton label are defined as photons which undergo Compton scattering followed by photoelectric absorption.

	Annihilation Photon 1	Annihilation Photon 2	Prompt Gamma	Count	Sensitivity
Group 1	Photoelectric	Photoelectric	Compton	18,908	0.06 %
Group 2	Photoelectric	Photoelectric	Non-Compton	169,471	0.51 %
Group 3	Compton	Compton	Non-Compton	2,036,264	6.13 %
Group 4	Compton	Compton	Compton	226,707	0.68 %
Group 5	Compton	Photoelectric	Compton	130,092	0.39 %
Group 6	Compton	Photoelectric	Non-Compton	1,168,638	3.52 %
Group 7	No LOR can be drawn		Compton	2,963,688	8.92 %
Total Decays: 33,249,180					

TABLE III:

General performance metrics of identical systems with varied crystal bin sizes. The surviving DCSc refer are in relation to the case with no crystal binning (arbitrary granularity).

Crystal Binning	Surviving DCSc	RMSE	MAE
1 mm	74.7%	584.3	6.8
2 mm	58.5%	721.1	9.5
4 mm	35.8%	727.3	12.2
8 mm	16.2%	610.9	15.3